nature communications

Article

https://doi.org/10.1038/s41467-025-61411-y

# Amorphous/crystalline $HTiNbO_{5-X}$ membranes for efficient confined flow synthesis of acetate ester flavours

Received: 4 February 2025

Accepted: 19 June 2025

Published online: 02 July 2025

Check for updates

Zhenyuan Fang[1,2,3,8], Xiang Li[2,8], Yajie Bai[4,8], Yuhui Zhang[3], Guandi He[2], Shuai Pang[3], Fan Xia[5,6], Daoling Peng[7], Xiqi Zhang[2,3] ✉ & Lei Jiang[1,2,3]

Ideal laminar membrane reactors (LMR) necessitate the rational construction of 2D nanoconfined channels and regulation of microenvironment. The intrinsic structure-activity relationship of laminar membrane reactors essentially remains unclear. Herein, amorphous/crystalline $HTiNbO_{5-X}$ nanosheets (NS) with abundant oxygen vacancy ($V_O$) are successfully prepared and stacked as 2D sub-nanoconfined membrane flow reactors with different interlayer spacings. When the interlayer spacing is decreased to 11.0 Å, the representative $HTiNbO_{5-X}$ membrane exhibits impressive conversion of ≈100% within 26.6 s and turnover number of up to 306.42 for the esterification of benzyl alcohol at 23 °C. The combination of structural characterizations and theoretical calculations reveals that the synergistic effect of $V_O$ and sub-nanoscale confinement greatly promotes the adsorption and orbital symmetry matching of reactants, and reduces the overall energy barrier. Furthermore, the $HTiNbO_{5-X}$ LMR is accessible for other alcohol derivatives, indicating the efficient and green synthesis of acetate ester flavours under mild conditions. This work demonstrates the promising potential of the metal oxide nanosheets to create inorganic laminar membrane reactors for continuous organic synthesis.

Efficient, environmental, and economically viable chemical processes or methodologies are in great demand for those widely used organic compounds. Acetate esters (e.g., benzyl acetate, anisyl acetate, cinnamyl acetate) are extensively used as flavours and fragrances in food, cosmetics and pharmaceuticals industries which are in high demand (as high as 10,000 tons per annum for benzyl acetate)[1]. Besides direct extraction from plant or fruit sources, these ester flavours are typically obtained through esterification reactions or enzymatic processes. Over the past few decades, various catalytic materials, including solid acids, ionic liquids and inorganic salts, have been explored to replace mineral acids (e.g., $H_2SO_4$) for serious corrosion and contamination issues[2,3]. Recently, the growing traction for sustainable processing has resulted in a transition from conventional batch reactors to advanced catalysis reactors[4]. Membrane reactors, as a continuous flow technology, offers many advantages including absence catalyst separation, precise temperature control and reduced power consumption[5].

Confinement can play a defining role in interface properties and chemical catalysis[6]. As the materials are assembled/confined to

[1]Key Laboratory of Bioinspired Smart Interfacial Science and Technology of Ministry of Education, School of Chemistry, Beihang University, Beijing, China. [2]Laboratory of Bio-inspired Smart Interface Science, Technical Institute of Physics and Chemistry, Chinese Academy of Sciences, Beijing, China. [3]Suzhou Institute for Advanced Research, University of Science and Technology of China, Suzhou, China. [4]College of New Energy, Ningbo University of Technology, Ningbo, China. [5]State Key Laboratory of Biogeology and Environmental Geology, Engineering Research Center of Nano-Geomaterials of Ministry of Education, Faculty of Materials Science and Chemistry, China University of Geosciences, Wuhan, China. [6]School of Mathematics and Physics, China University of Geosciences, Wuhan, China. [7]Key Laboratory of Theoretical Chemistry of Environment, Ministry of Education, School of Environment, South China Normal University, Guangzhou, China. [8]These authors contributed equally: Zhenyuan Fang, Xiang Li, Yajie Bai. ✉e-mail: xqzhang@mail.ipc.ac.cn

nanoscale, their geometric and electronic structures in the confined state operate as thermodynamically and kinetically more critical factors than those in the bulk state, which can result in unusual physicochemical and catalytic properties[7]. Over the past decade, tremendous efforts have been devoted to preparing various porous nanomaterials from 1D to 3D (e.g., carbon nanotubes, graphene oxide, metal-organic frameworks), while only a small portion of work have successfully constructed nanoconfined systems or materials[8–10]. For example, Al/Ni-Pt/Ti nanotube was reported to show remarkably high efficiency in nitrobenzene hydrogenation due to the instant transfer of intermediates and the tailored electronic properties of confined nanochannels[9]. However, these materials mainly participate in catalytic reactions through batch reactors and the reaction efficiencies are still limited by the disordered motion of molecules and the inefficient diffusion of molecules between the bulk solution and the nanochannels of porous materials, especially for molecular-scale channels[10]. Moreover, current study of catalytic materials are mainly focused on the design of nanomaterials with hierarchical channels and the degree of confinement for these systems are localized within several to tens of nanometers considering heat and mass transfer, and thereby the intrinsic structure–activity relationship of sub-nanoscale confinement has attracted intense interests[6].

In natural enzymes, reactants diffuse into the active sites with the binding sites and catalytic sites to break and form bonds[11]. The synergy of multiple sites contribute to their extremely high activity and selectivity. There is a great challenge to apply this concepts into membrane flow reactors with confined channels in sub-nanometer scale, even though it is at the forefront of catalytic chemistry. Recently, many 2D materials, such as graphene oxide (GO), covalent organic framework (COF), layered double hydroxide (LDH), and transition metal oxides/chalcogenides (TMO/C), have been employed for the fabrication of 2D material membranes, and these membranes have been effectively practiced in separation and purification[12–16]. Actually, 2D materials have atomic-level thicknesses and unique physicochemical properties, and they are also very promising platforms to develop new nanoconfined flow reactors for organic synthesis[17,18]. For instance, we have controlled the chemical structure of 2D graphene oxide membranes effectively, and realized rapid Knoevenagel condensation and synthesis of aspirin recently[19,20]. Through tuning the interlayer distances and interface properties of nanochannels, the intrinsic characteristics of the reaction, e.g., mass transfer, reaction kinetics, and selectivity, can be effectively dominated under mild process conditions. It is thus attractive to implement laminar membrane reactors for continuous pharmaceutical and fine chemical synthesis[18]. However, the difficulty in preparing of uniform, large sized and ultrathin 2D nanosheets (e.g., COF, LDH) to create effective confined nanochannels greatly restrict the development of LMR[17]. In addition, the currently reported 2D materials lack proper and stable catalytic active sites for specific reactions (esterification in this work). In contrast to 2D carbonaceous materials like GO with abundant oxygen-containing groups, 2D metallic compounds (e.g., TMO) are difficult to modulate the microenvironment nearby catalytic sites[21]. Oxygen vacancies in TMO have demonstrated to be beneficial for many applications due to their unsaturated coordination and distinct reactivity[22]. However, achieving precise control of these defects remains a significant challenge, and the role of vacancies to the adsorption and activation of reactants, especially under 2D confined conditions, remains largely unknown[23].

Here, we report an outstanding laminar membrane reactors prepared by amorphous/crystalline $HTiNbO_{5\text{-}X}$ nanosheets enriched with oxygen vacancies, which enables rapid and efficient synthesis of acetate ester flavours (Fig. 1a, b). The Brønsted acid sites and oxygen vacancies are engineered onto the $HTiNbO_{5\text{-}X}$ nanosheets by acid etching (Fig. 1c–f). The sub-nanoconfined channels of $HTiNbO_{5\text{-}X}$ membranes are controlled from 14.4 to 11.0 Å by mild thermal treatment (Fig. 1g, h). As a result, alcohol molecules move through the sub-nanoconfined channels directionally and react with acetic anhydride ($Ac_2O$) molecules efficiently under mild conditions (Fig. 1i, j). When the interlayer spacing is decreased to 11.0 Å, the esterification of benzyl alcohol (BnOH) is realized with conversion of ≈ 100% in an unparalleled short time and turnover number (TON) of up to 28 times higher than that of bulk reaction at 23 °C (Fig. 1k). The synergy of multiple sites and confined spatial structures are realized in this bioinspired LMR, contributing to the modulation of reactant adsorption, molecular polarization, orbital symmetry matching and reaction thermodynamics. We have adjusted the membrane thicknesses, pressure difference, reaction temperatures and reactant concentrations, and further expanded the substrate scope and stability test, proving the rationality and superiority of the laminar membrane reactors to conventional batch reactors.

## Results

### The synthesis and characterization of $HTiNbO_{5\text{-}X}$ membrane

The ultrathin $HTiNbO_{5\text{-}X}$ NS were successfully obtained by calcination, acid etching, and exfoliation steps (Fig. 1b)[22,24]. It is noteworthy that $KTiNbO_5$ was treated in HCl aqueous solution for multiple times. This step not only facilitated sufficient protonation of $KTiNbO_5$ introducing Brønsted acid sites, but also created abundant oxygen vacancy ($V_O$)[25,26]. After that, a small amount of tetrabutylammonium cations ($TBA^+$) was used to expand the interlayer spacing of bulk $HTiNbO_{5\text{-}X}$ for exfoliation and to stabilize the interlayer distances of $HTiNbO_{5\text{-}X}$ membrane. The morphology of the samples was investigated by scanning electron microscopy (SEM), transmission electron microscopy (TEM) and atomic force microscopy (AFM). Both $KTiNbO_5$ and bulk $HTiNbO_{5\text{-}X}$ presented closely compacted layered structure (Supplementary Fig. 1). The size of these lamellar particles reaches several micrometers. As shown in Supplementary Fig. 2, the colloidal dispersions of the $HTiNbO_{5\text{-}X}$ NS are stable over one month, implying its well dispersion and uniformity. The TEM images of $HTiNbO_{5\text{-}X}$ NS depicted in Fig. 1c and Supplementary Fig. 3 clearly show a large area 2D ultrathin nature and the average size is about 0.5 ± 0.1 μm, indicating its suitability for constructing laminar membrane reactors. Energy-dispersive X-ray spectroscopy (EDX) elemental mapping of the $HTiNbO_{5\text{-}X}$ nanosheets reveals the uniform distributions of Ti, Nb and O across the sample, confirming the successful synthesis of $HTiNbO_{5\text{-}X}$ nanosheets (Supplementary Fig. 4 and Supplementary Table 1). The thickness of the exfoliated $HTiNbO_{5\text{-}X}$ nanosheets was measured by AFM with the corresponding height profile (≈1.2 nm) presented in Fig. 1d. Considering the thickness of single-crystal nanosheet and surface adsorption of solvents or guest species ($TBA^+$ cations), the as-prepared $HTiNbO_{5\text{-}X}$ nanosheets consist of monolayer[22,24]. The microstructure of the samples were also investigated by powder X-ray diffraction (XRD). In Supplementary Fig. 5a, all the characteristic peaks of the $KTiNbO_5$ are indexed to a layered structure with an orthorhombic crystal $KTiNbO_5$ phase (JCPDS 72-1076). Interestingly, the characteristic diffraction peaks for bulk $HTiNbO_{5\text{-}X}$ show obvious shift after replacement of $K^+$ with $H^+$, while the intensity of $HTiNbO_{5\text{-}X}$ nanosheets become very weak. The weak and absence of characteristic peaks for $HTiNbO_{5\text{-}X}$ nanosheets indicates the decreased crystallinity and presence of the amorphous phases[27,28].

The surface properties were identified by the Fourier transform infrared (FTIR), pyridine FTIR spectra and $NH_3$ temperature programmed desorption (TPD). As shown in Supplementary Fig. 5b, it was revealed that both $HTiNbO_{5\text{-}X}$ NS and bulk $HTiNbO_{5\text{-}X}$ had two distinctive signals at 3600–3100 $cm^{-1}$ and 1600 $cm^{-1}$ which can be assignable to the stretching modes and bending modes of hydroxyl groups (OH), respectively[29–33]. This indicates that there is a considerable amount of hydroxyl groups on the surfaces of $HTiNbO_{5\text{-}X}$ nanosheets. The acidity distribution was investigated using pyridine FTIR spectroscopy. As shown in Fig. 1e and Supplementary Fig. 6a–c,

https://doi.org/10.1038/s41467-025-61411-y

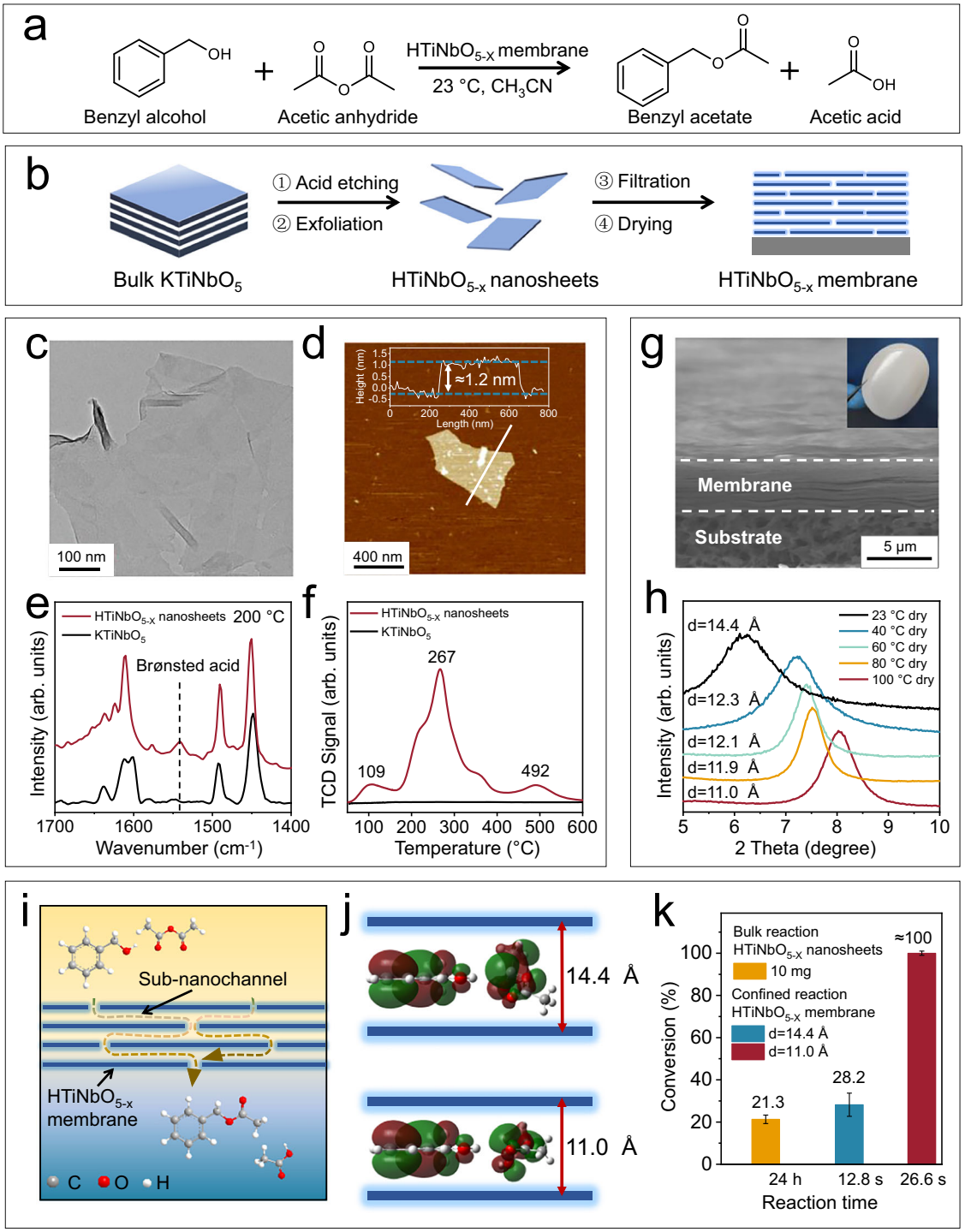


**Fig. 1 | The synthesis method and structural diagrams of $HTiNbO_{5-X}$ membranes. a** The esterification of benzyl alcohol with acetic anhydride catalyzed by $HTiNbO_{5-X}$ membranes in $CH_3CN$ at 23 °C. **b** Fabrication of the $HTiNbO_{5-X}$ nanosheets and $HTiNbO_{5-X}$ membrane. **c** TEM image of $HTiNbO_{5-X}$ nanosheets. **d** AFM image and corresponding height profile of $HTiNbO_{5-X}$ nanosheets. **e** Pyridine IR spectra and **f** $NH_3$ TPD profiles of $HTiNbO_{5-X}$ nanosheets and $KTiNbO_5$. **g** Cross-sectional SEM image of $HTiNbO_{5-X}$ membrane (Inset show the photograph of the as-prepared $HTiNbO_{5-X}$ membrane). **h** XRD patterns measured for the reaction-state of $HTiNbO_{5-X}$ membranes obtained by different annealing temperatures. **i** Scheme of the $HTiNbO_{5-X}$ membrane reactor showing the esterification of benzyl alcohol with acetic anhydride. Driven by the pressure difference, the alcohol and anhydride molecules react efficiently within 2D nanochannels. **j** Symmetry matching between the HOMO of the benzyl alcohol and the LUMO of protonated acetic anhydride in the nanochannels with different interlayer spacing. **k** Comparison of the conversion and reaction time for bulk and confined reactions. Confined reaction condition: $HTiNbO_{5-X}$ membrane, benzyl alcohol (0.2 M) and acetic anhydride (0.3 M) in $CH_3CN$ (10 mL) at 23 °C. Bulk reaction condition: $HTiNbO_{5-X}$ nanosheets (10 mg), benzyl alcohol (0.2 M) and acetic anhydride (0.3 M) in $CH_3CN$ (10 mL) at 23 °C for 24 h. Error bars represent standard deviation of three measurements.

the absorption bands at 1445–1454 $cm^{-1}$ indicate the presence of coordinately bonded pyridine at Lewis acid sites, while the bands at 1546 $cm^{-1}$ are assigned to pyridine adsorbed at Brønsted acid sites[32–34]. The pyridine FTIR spectra prove that $HTiNbO_{5-X}$ NS have both Lewis acid and Brønsted acid sites. Even after evacuation at 200 °C, the absorption bands of Brønsted acid sites could still be detected and the Brønsted/Lewis acid ratio is 0.184 for $HTiNbO_{5-X}$ nanosheets, indicating these samples have good stability and catalytic potential (Supplementary Table 2).The overall acidity of the samples was further probed by $NH_3$ TPD (Fig. 1f and Supplementary Fig. 6d). For bulk $HTiNbO_{5-X}$, desorption of $NH_3$ occurred from 150 to 650 °C, indicating a wide range of acid sites[33,34]. The broad desorption signal could be divided into two peaks centered at 208 and 525 °C, representing sites of medium and strong acidity. For $HTiNbO_{5-X}$ nanosheets, the peaks in the range of 200-400 °C belongs to sites of medium acidity, and peaks centered at 492 °C represents strong acidity sites. The strong acidity sites should be ascribed to Brønsted acid sites at Ti(OH)Nb sites, and a slight decrease of peaks centered at 492 °C is found for $HTiNbO_{5-X}$ nanosheets since bulk $HTiNbO_{5-X}$ was soaked in TBAOH dilute solution for exfoliation. The overall acidity of these samples was calculated in the following order: $KTiNbO_5$ (0.013 mmol/g) <$HTiNbO_{5-X}$ nanosheets (3.885 mmol/g) <bulk $HTiNbO_{5-X}$ (4.567 mmol/g). These results consolidate that $HTiNbO_{5-X}$ nanosheets have abundant Brønsted acid sites and Lewis acid sites induced by acid treatment.

The 2D $HTiNbO_{5-X}$ laminar membranes were prepared by stacking $HTiNbO_{5-X}$ nanosheets onto a nylon substrate through vacuum filtration (Supplementary Fig. 7). It was demonstrated that the interlayer spacing of the layered metal oxide can be adjusted by changing the cations and thermal treatment[18]. The protons are partially exchanged by appropriate organic cations ($TBA^+$), leading to chemical exfoliation of bulk $HTiNbO_{5-X}$ and modulation of interlayer distance of the $HTiNbO_{5-X}$ membranes. The as-prepared membranes were air dried at room temperature (RT) or thermally treated in vacuum oven at certain temperature, which are named Y °C dry (where Y is the corresponding temperature). In the Supplementary Fig. 8a, the XRD patterns of $HTiNbO_{5-X}$ membranes in dry-states exhibit sharp (002) diffraction peaks, which also indicates that the $HTiNbO_{5-X}$ membranes possessed a highly ordered stacking arrangement. Using the Bragg's law, the interlayer distances of the dried $HTiNbO_{5-X}$ membranes were decreased from 1.37 nm to 1.02 nm after increasing the heat-treatment temperature. With increasing calcination temperature, the $H_2O$ gradually evaporates from the interlayer and the $TBA^+$ cations can turn into different geometric configuration and sizes (Supplementary Fig. 9). This can be evidenced by the weakening of the infrared absorption peak at 3600–3100 $cm^{-1}$ and 1600 $cm^{-1}$ with increasing temperature (Supplementary Fig. 8b). As displayed in Supplementary Figs. 10 and 11, both SEM images and TEM images of the cross-section of membranes revealed the well-ordered lamellar structure of the $HTiNbO_{5-X}$ membrane. In Supplementary Fig. 11, the alternating dark and light pattern shows the average thickness of one layer of lamellar is 0.7 nm, which matches the theoretical thickness of the $HTiNbO_{5-X}$ nanosheet. The esterification of benzyl alcohol with acetic anhydride was carried out as the model reaction to study the catalytic properties of $HTiNbO_{5-X}$ membranes. Before the reaction, corresponding molecular sizes are all predicted (Supplementary Figs. 9, 12). Through comparison and analysis, the thicknesses of molecules involved in esterification are all less than that of $TBA^+$ cations. Thus, the membranes are effectively developed into different interlayer spacings allowing the continuous flow of reactants and products.

### The catalysis performance of $HTiNbO_{5-X}$ membrane

The esterification of benzyl alcohol with acetic anhydride was carried out in a microfiltration device (Supplementary Fig. 7b). After clamping $HTiNbO_{5-X}$ membranes, the reaction solution of alcohol and acetic anhydride permeates through the $HTiNbO_{5-X}$ membranes driven by the pressure difference (0.9 atm), and the reactants react within the two-dimensional sub-nanochannels at RT, and the products flow into the collection bottle with the solvent. As mentioned above, five types of $HTiNbO_{5-X}$ membranes with different interlayer distances were utilized for the confined benzyl acetate synthesis. After more than 12 h of reaction, the reaction-state interlayer spacing of membranes was tested by XRD immediately. In the Fig. 1h and Supplementary Table 3, the interlayer spacings of the reaction-state $HTiNbO_{5-X}$ membranes decrease monotonically, and are calculated to be 14.4, 12.3, 12.1, 11.9 and 11.0 Å by Bragg's law, respectively. The XRD patterns of $HTiNbO_{5-X}$ membranes in both dry-state and reaction-state exhibit strong diffraction peak (002), confirming that their orderly layered structures are maintained in the process of reactions. The composition and conversion efficiency of the permeation solution was determined by $^1H$ NMR spectroscopy (Fig. 2a and Supplementary Fig. 13). Surprisingly, the characteristic signals of benzyl alcohol faded away along with the interlayer spacings decreasing, whereas those for benzyl acetate enhanced and the conversion of benzyl alcohol gradually improved from 28.2% to 100% (Fig. 2a, b). When the interlayer spacing turned to 11.0 Å, the characteristic signals of benzyl alcohol completely disappeared, and nearly complete conversion ($\approx$100%) was achieved at 23 °C in a very short reaction time of 26.6 s. Additionally, the flow volume of the reaction solution was observed to be linear with time, reflecting that the volumetric flow rate was steady (Supplementary Fig. 14). It was found that the velocity of the permeation solution gradually decreased with the decreasing of the interlayer spacing of the $HTiNbO_{5-X}$ membranes, whereas reaction time ($t_R$) were calculated to be increased from 12.8 s to 26.6 s. The slightly increase in reaction time is attributed to the more severe spatial constraints to the reaction solution.

Considering that the reaction time increases with the decrease of interlayer spacings, the increased conversion in $HTiNbO_{5-X}$ membranes may be related to both reaction time and confinement effects. Thereby, the reaction time of reaction solution in the $HTiNbO_{5-X}$ laminar membranes were further studied by adjusting the membrane thicknesses, and the corresponding conversions of benzyl alcohol were tested. The $HTiNbO_{5-X}$ membranes with different loadings were thermally treated in same temperature (60 °C dry) to maintain at a nearly constant interlayer spacing (d = 12.1 Å) but different thicknesses in Fig. 2c. The volume of the reaction mixture passing through is still linearly related to reaction time, and the velocity was decreased with the increased membrane thicknesses (Supplementary Fig. 15). As the thicknesses increased from 2.6 μm to 10.4 μm, the conversions of benzyl alcohol improved from 23.6% to 100%, but the reaction time greatly increased from 7.9 s to 63.5 s. This is mainly attributed to the weakened confinement effect. Moreover, the effect of reaction times on the conversion is further investigated by adjusting the operating pressure difference (Supplementary Fig. 16). When the pressure difference decreased to 0.3 atm and 0.6 atm, the reaction mixture had a lower flux and a higher reaction time through the $HTiNbO_{5-X}$ membranes (d = 14.4 Å). Even though the reaction time greatly increased to 27.5 s and 48.1 s, the conversions of benzyl alcohol only improved to 53.2% and 65.6% (Supplementary Fig. 16b). This results indicates that extending reaction time slightly increase benzyl alcohol conversion, but reducing interlayer spacing significantly promotes esterification reactivity. Besides, the confined reactions of $HTiNbO_{5-X}$ membranes are also performed at different temperatures in Supplementary Fig. 17. When the temperature comes to 30 °C, the conversion was greatly improved from 20.4% for $HTiNbO_{5-X}$ membranes (d = 14.4 Å) to 58.3% for $HTiNbO_{5-X}$ membranes (d = 11.0 Å) in Supplementary Figs. 18, 19. But the reaction time was calculated to show slight difference from 13.7 s to14.3 s. These results all proved that the

https://doi.org/10.1038/s41467-025-61411-y

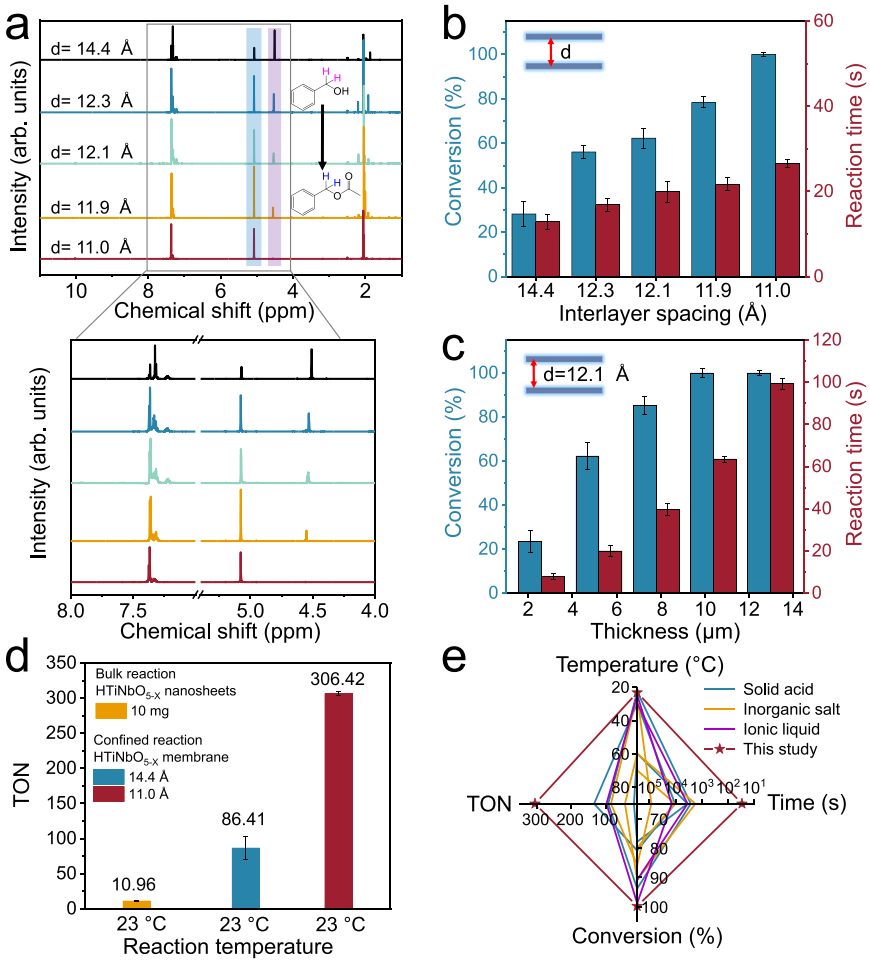


**Fig. 2 | Catalytic performance assessment of the $HTiNbO_{5-X}$ membranes. a** $^1H$ NMR spectra measured for the permeation solution through $HTiNbO_{5-X}$ membranes with different interlayer spacing (d). **b** The conversion and reaction time for $HTiNbO_{5-X}$ membranes with different interlayer spacing. **c** The conversion and reaction time for $HTiNbO_{5-X}$ membranes (interlayer spacing of 12.1 Å) with different thicknesses. **d** Comparison of turnover number (TON) for bulk reaction and confined reaction. Confined reaction condition: $HTiNbO_{5-X}$ membrane, benzyl alcohol (0.2 M) and acetic anhydride (0.3 M) in $CH_3CN$ (10 mL) at 23 °C. Bulk reaction condition: $HTiNbO_{5-X}$ nanosheets (10 mg), benzyl alcohol (0.2 M) and acetic anhydride (0.3 M) in $CH_3CN$ (10 mL) at 23 °C for 24 h. **e** Comparison of reaction temperature, reaction time, conversion and TON of $HTiNbO_{5-X}$ membranes with those of other catalysts. All the references associated with this plot are tabulated in Supplementary Table 4. Error bars represent standard deviation of three measurements.

prolonged reaction time has a slight impact on the conversion, whereas interlayer spacing has a more significant impact.

In comparison, $HTiNbO_{5-X}$ nanosheets were also utilized as heterogenous catalysts for benzyl acetate synthesis. The bulk reaction was conducted under the same conditions. As shown in the Figs. 1k, 2d, the catalytic performance for $HTiNbO_{5-X}$ nanosheets is limited by the disordered motion of molecules. Through increasing the reaction time from 24 h to 48 h, the reaction efficiencies of $HTiNbO_{5-X}$ nanosheets in the bulk system are raised from 21.3% to 38.4%. However, this enhancement is still inferior to that of the confined system. The catalyst dosage of $HTiNbO_{5-X}$ NS in bulk condition is 10 mg, whereas that of $HTiNbO_{5-X}$ membranes in confined system is calculated to be only 1.68 mg. Combining with the overall acidity probed by $NH_3$ TPD, the turnover number for $HTiNbO_{5-X}$ membranes at 23 °C increases from 86.41 to 306.42 as the interlayer spacings decrease (Fig. 2d). The optimum results are about 28 times higher than that of bulk reaction (10.96). Over the past two decades, various homogeneous and heterogeneous catalysts, including solid-acids, inorganic salts and ionic liquids, have been applied to benzyl acetate synthesis (Supplementary Table 4). In order to achieve a better catalytic performance, most of the reported works adopted high reaction temperature or extended reaction time or catalyst dosages, and there were few studies for the efficient synthesis of benzyl acetate (Fig. 2e). Ulteriorly, three types of commercial solid acid catalysts, HZSM-5 (zeolite molecular sieves), $H_3O_{40}PW_{12}{\cdot}xH_2O$ (heteropoly acids) and amberlyst-15 (acidic resins), were purchased for comparison. Under the premise of the same concentrations, the performances of $H_3O_{40}PW_{12}{\cdot}xH_2O$ and amberlyst-15 are superior to HZSM-5 and

$HTiNbO_{5-X}$ nanosheets in the bulk reaction (Supplementary Table 5). This is mainly attributed to their stronger acidity. However, the $H_3O_{40}PW_{12}{\cdot}xH_2O$ was dissolved in the product benzyl acetate, and the collected benzyl acetate exhibits a light golden colour (Supplementary Fig. 46). The Amberlyst-15 ion-exchange resins were easily separated from solutions, but the collected benzyl acetate shows a noticeable orange color after reaction. This may be due to the unstable structure of the amberlyst-15[35,36]. These results demonstrate the advantages of $HTiNbO_{5-X}$ membranes in catalyst separation and product purity.

## Structural analysis of $HTiNbO_{5-X}$ nanosheets

Since the $HTiNbO_{5-X}$ membranes are fabricated by vacuum filtration of $HTiNbO_{5-X}$ nanosheets, the origin of its outstanding performance should be related to the structures of $HTiNbO_{5-X}$ nanosheets. To gain further insights into the electronic structure and chemical states for

$HTiNbO_{5-X}$ membranes, several other analytical techniques, including X-ray photoelectron spectroscopy (XPS) and Raman spectra, were performed. The XPS data for $KTiNbO_5$ shows characteristic Ti 2p peaks for $Ti^{4+}$ and Nb 3 d peaks for $Nb^{5+}$, but in the case of bulk $HTiNbO_{5-X}$ and $HTiNbO_{5-X}$ nanosheets these peaks shift to lower binding energy (Supplementary Fig. 20). This likely results from the presence of $Nb^{4+}$ and $Ti^{3+}$ due to the acid etching[37–40]. In addition, O 1 s can be divided into two fitting peaks. As shown in Supplementary Fig. 21, the main peak of lattice oxygens are shifted from 530.3 eV to 529.7 eV, which can be ascribed to the oxygen defects or vacancies present in the lattice of $HTiNbO_{5-X}$[40]. The shoulder peak at 531.3 eV typically corresponds to adsorbed oxygen around oxygen vacancy sites[27,38]. As for $HTiNbO_{5-X}$ membranes, the position of these peaks hold the stable during the vacuum thermal treatment (Supplementary Fig. 22). Notably, when the temperature increases, the content of oxygen vacancies gradually decreases from 29.2% to 22.5% (Supplementary Table 6). To gain insights into the role of oxygen vacancy, the nanosheets of $HTiNbO_{5-X}$ membranes after thermal treatment at 100 °C were collected for bulk reaction. Under the same dosages, the performances of the nanosheets decreases from 21.3% to 8.6%. Thus, it can be confirmed that oxygen vacancies play a key role during the reaction process. The Raman spectra were further collected to identify structural changes of $HTiNbO_{5-X}$ membranes, because it is very sensitive to the structure and bond order of metal oxides, especially in the region relating to metal-oxygen stretching modes (Supplementary Fig. 23)[41,42]. The Raman shift in the range of 590–720 $cm^{-1}$ belongs to the stretching vibration of the Ti–O–Ti bond in the $TiO_6$ octahedron, and the shift in the range of 480-570 $cm^{-1}$ belongs to the stretching vibration of the Nb–O–Nb bond in the $NbO_6$ octahedron[41]. It is worth noting that the peaks for $HTiNbO_{5-X}$ nanosheets and $HTiNbO_{5-X}$ membranes both showed evidently broad and enhanced absorption at around 885 and 934 $cm^{-1}$, and these peak is typically regarded as the unsaturated Ti=O and Nb=O surface groups, compared with the shift of $KTiNbO_5$. The above results suggest the prepared $HTiNbO_{5-X}$ nanosheets have partial structural changes which can be attributed to acid etching, and thereby the metal occupation at tetrahedral and octahedral sites might have slight differences[38,41].

Ulteriorly, the selected area electron diffraction (SAED) pattern of $HTiNbO_{5-X}$ nanosheets shows clear diffraction rings (Fig. 3a), indicating that the $HTiNbO_{5-X}$ nanosheets are etched by hydrochloric acid resulting partially disordered atomic arrangement[26,27]. Notably, the High-resolution TEM image (HRTEM) reveals that the prepared $HTiNbO_{5-X}$ nanosheets are typically composed of amorphous and crystalline domains (Fig. 3b). The amorphous structural regions are relatively larger than crystalline regions, demonstrating the low crystallinity of $HTiNbO_{5-X}$ nanosheets (Supplementary Fig. 24).This is consistent with XRD results (Supplementary Fig. 5a). Additionally, low-temperature electron paramagnetic resonance (EPR) was employed to validate the generation of $Nb^{4+}$/ $Ti^{3+}$/$V_O$ pairs since this technology was very sensitive to paramagnetic species containing unpaired electrons (Fig. 3c and Supplementary Fig. 25). From Fig. 3c, it can be seen that $HTiNbO_{5-X}$ nanosheets show distinctive EPR signals at about g = 2.253 and g = 2.028 assigned to $Nb^{4+}$ and $Ti^{3+}$, respectively[43–45]. In Supplementary Fig. 25, signal with g = 4.252 could be assigned to $Nb^{3+}$ species[43]. After that, the indicator of g values at 2.067 and 2.002 should be attributed to the corresponding oxygen vacancies in the lattices[37]. The abundant oxygen vacancies break the octahedral symmetry of $NbO_6$ and $TiO_6$, which derive $Nb^{4+}$ and $Ti^{3+}$ with unpaired electron. Besides, the thermogravimetric analysis (TGA) curve shows that the $HTiNbO_{5-X}$ nanosheets has a small mass loss in nitrogen atmosphere, but the decomposition rate is decreased in oxygen atmosphere (Fig. 3d). This feature also serves as an indirect evidence for the existence the oxygen vacancy, in agreement with the XPS, Raman, EPR and HRTEM findings above. The created oxygen defects as highly active low-coordination sites can break the inherent crystal arrangement causing amorphous domains and readjust the local electron structure (Supplementary Fig. 26)[28,29]. As such, the adsorption and activation of reactants may be optimized and thus boosting the reaction performance.

## Theoretical calculation for catalytic mechanism

In view of the extensive oxygen vacancies in the confined nanochannel, an effective modulation of interface properties of $HTiNbO_{5-X}$ membranes is expected. Before theoretical calculations, we undertook Raman studies to understand the intricate interaction between reactant molecules and oxygen vacancies (Supplementary Fig. 27). The strong electrophilic properties of the oxygen vacancy are beneficial to its adsorption with oxygen containing groups of acetic anhydride and benzyl alcohol. As the experiment progresses, benzyl alcohol and acetic anhydride molecules gradually move through and react within the $HTiNbO_{5-X}$ membranes. In Supplementary Fig. 27, the peak of Nb=O gradually shifted from 940 $cm^{-1}$ to 948 $cm^{-1}$, whereas other peaks show no obvious shift. This can be attributed to the adsorption of reactant molecules at oxygen vacancies around Nb sites[21]. Therefore, the oxygen vacancies at Nb sites were considered for calculation[29,30]. The potential distribution is explored by electrostatic potential simulation to study the surface electronic state like bonding nature of $HTiNbO_{5-X}$ nanosheets with reactant molecules (Supplementary Fig. 26). The obvious potential difference can be seen around the oxygen vacancy, revealing the formation of local polarization and constructing strong local electric field[46,47]. The strong electrophilic properties of the oxygen vacancy are beneficial to molecular polarization and transition state stabilization[48]. Thus, the adsorption energies ($E_{ads}$) of BnOH and $Ac_2O$ intercalating between the nanosheets of $HTiNbO_5$ (no defects) and $HTiNbO_{5-X}$ were both calculated using density functional theory (DFT). Considering the reaction-state interlayer spacing (11.0 Å) and thickness of monolayer nanosheets (0.7 nm), the interlayer free distances ($d_{free}$) of 4 Å were taken to simulate the adsorption behavior of confined reaction (Supplementary Figs. 28, 29). For bulk reaction, the 40 Å vacuum space is used to simulate the surface environment, ensuring that the slab model remains sufficiently isolated[15,49]. This distance is large enough compared to the size of the reactants (benzyl alcohol: 4.02 × 7.00 × 9.10 Å; acetic anhydride: 4.01 × 5.34 × 8.72 Å) in the Supplementary Fig. 12. The calculated results proved that the adsorption energy ($d_{free}$ = 40 Å) of BnOH and $Ac_2O$ in $HTiNbO_{5-X}$ were both higher than that of $HTiNbO_5$, indicating the strong adsorption on oxygen vacancy ($E_{ads}$ = −0.800 eV for BnOH, $E_{ads}$ = −0.584 eV for $Ac_2O$). Interestingly, these energies were further improved greatly when the $d_{free}$ decreased to 4 Å, especially for $HTiNbO_{5-X}$ ($E_{ads}$ = −1.270 eV for BnOH, $E_{ads}$ = −1.133 eV for $Ac_2O$). Specifically, benzyl alcohol and acetic anhydride exhibit strong electrostatic interactions with oxygen vacancies in $HTiNbO_{5-X}$ membranes through benzene ring, hydroxyl oxygen and carbonyl oxygen, whereas in $HTiNbO_5$ membranes, the interactions are mediated by weak hydrogen bonds (Fig. 3e, f, Supplementary Figs. 28, 29). Therefore, the synergistic effects of oxygen vacancies and confinement effect are identified, which benefits to the adsorption and activation of the reactants.

ATR FTIR measurements were performed to gain further insights into the reaction progression (Supplementary Fig. 30). These investigations enabled the monitoring of the chemical transformations occurring within the $HTiNbO_{5-X}$ membranes. After a specific time of reaction (0 h, 0.5 h, 1 h and 12 h), reaction-state membranes were collected and tested by ATR FTIR spectra immediately. For acid anhydride, the peaks at 1756 $cm^{-1}$ and 1828 $cm^{-1}$ are assigned to the stretching mode of C = O. As the experiment progresses, these peaks are red shifted to 1752 $cm^{-1}$ and 1822 $cm^{-1}$, which should attribute to the protonation of acetic anhydrides[50,51]. After 12 h of confined flow reaction, benzyl acetate (product) is enriched inside the membrane. The stretching mode of C = O and C-O for the ester is significantly enhanced at around 1709 $cm^{-1}$ and 1232 $cm^{-1}$. These are direct observations of reaction intermediates and products.

https://doi.org/10.1038/s41467-025-61411-y

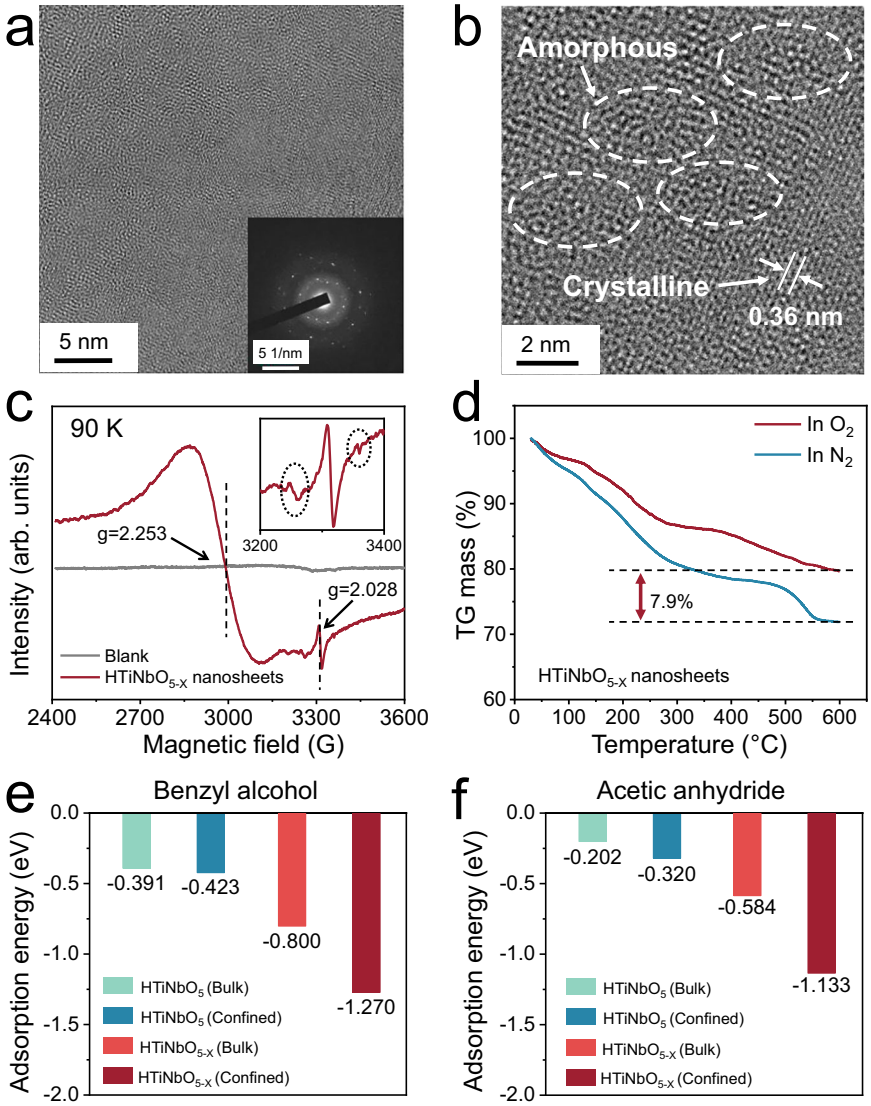


**Fig. 3 | The adsorption behaviour of reactants within $HTiNbO_{5-X}$ membranes.** **a** TEM (Inset show the SAED pattern) and **b** HRTEM images of $HTiNbO_{5-X}$ nanosheets. **c** Low temperature EPR spectra of $HTiNbO_{5-X}$ NS. **d** Thermogravimetric curve of $HTiNbO_{5-X}$ NS in nitrogen and oxygen environment. **e** The adsorption energy of BnOH intercalating into the interlayer of $HTiNbO_5$ membranes and $HTiNbO_{5-X}$ membranes in bulk and confined states. **f** The adsorption energy of $Ac_2O$ intercalating into the interlayer of $HTiNbO_5$ membranes and $HTiNbO_{5-X}$ membranes in bulk and confined states. For comparison, the different interlayer free distances represent bulk states (40 Å) and confined states (4 Å). More details in supplementary information.

To reveal the underlying mechanisms of bulk and confined reactions, we investigated the free energy of the reaction paths through DFT calculations, based on the spatial confinement and the chemical structure of catalysts. The esterification in both the bulk and confined systems is divided into the following three steps, that is protonation, nucleophilic addition, and deprotonation. As illustrated in Supplementary Fig. 31, Brønsted acid sites on the surface of $HTiNbO_{5-X}$ nanosheets are employed as the proton donor, and the acetic anhydrides are easily protonated to the first intermediate (IM1) in both bulk and confined systems due to the good electronegativity of carbonyl oxygen. This could promote the electron-withdrawing property of oxygen atom weakening C-O bond, and further increases the positive charge on the carbon atom. Subsequently, the lone pair electrons of alcohol hydroxyl oxygen in benzyl alcohol attack the empty antibonding $\pi^*$ orbital of carbon atom to generate the second intermediate (IM2) through the first transition state (TS1). Notably, the Gibbs free energies from IM1 to TS1 are demonstrate as the maximum energy barrier in both the bulk and confined systems. The energies from IM1 to TS1 for the bulk and confined conditions respectively are calculated to be 42.0 kJ/mol and 28.8 kJ/mol, demonstrating a great decrease of the energy barrier (Fig. 4c, d). For the bulk reaction, the energy barrier mainly derives from the disordered motion and inefficient diffusion of molecules to active sites reflected by its low turnover number (Supplementary Fig. 35). In order to obtain higher reaction efficiency, the reaction time and temperature need to be increased (Fig. 4a, b). For the confined reaction, as the channel dimension decreases to nanoscale (especially angstrom scale), the disordered motions of reactant molecules are greatly constrained. In nucleophilic addition reactions, the symmetry match of molecular orbitals determines whether the reaction can proceed efficiently, mainly involving the direction of orbital interaction between the nucleophile and the substrate. This has been confirmed by the higher conversion rate of the confined reaction (Fig. 4b). The conversion are raised from 7.8% (24 h) in bulk system to 56.2% in confined system at 10 °C. This value is close to the conversion (58.4%) of bulk reaction at 60 °C (Fig. 4a). As shown in the Supplementary Fig. 32, the reactants are reorganized and become more orderly within the 2D confined sub-nanochannels. When the interlayer distance decreases from 14.4 Å to 11.0 Å, the best

https://doi.org/10.1038/s41467-025-61411-y

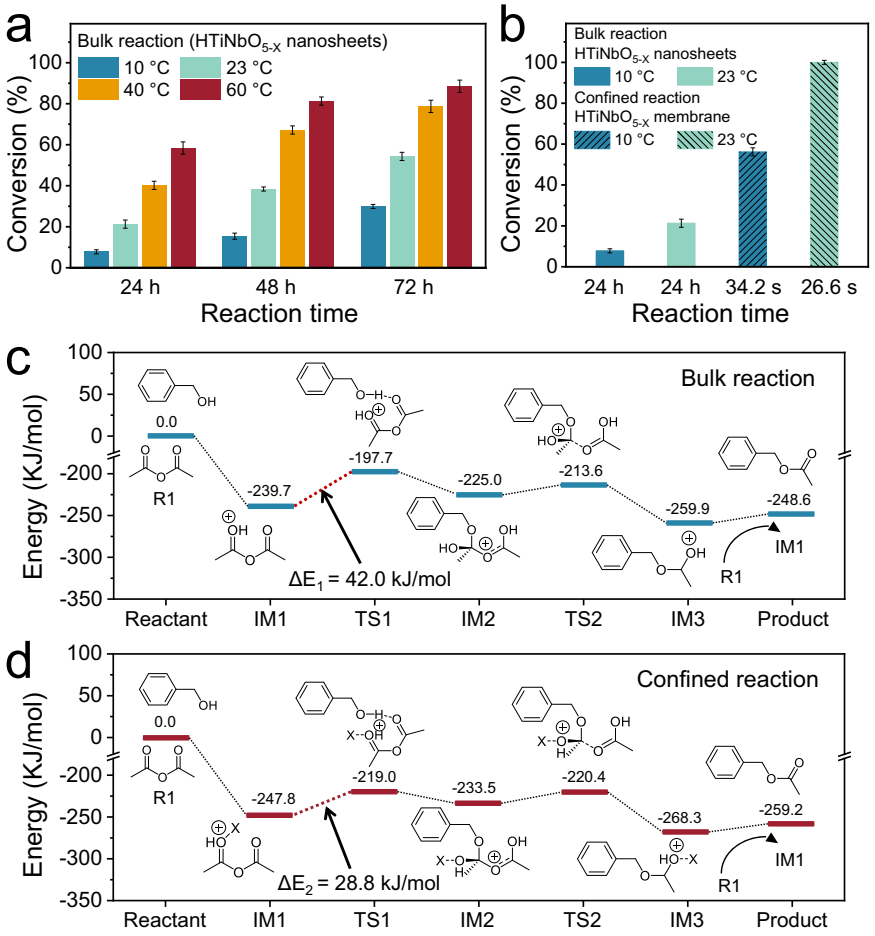


**Fig. 4 | DFT calculations of the reaction pathways over the bulk and confined reactions. a** Bulk reaction at different temperatures using $HTiNbO_{5-X}$ nanosheets as the catalyst. **b** Comparison of the conversion and reaction time of bulk and confined reactions at 10 °C and 23 °C. Bulk reaction condition: $HTiNbO_{5-X}$ nanosheets (10 mg), alcohol (0.2 M) and acetic anhydride (0.3 M) in $CH_3CN$. Confined reaction condition: $HTiNbO_{5-X}$ membrane (d = 11.0 Å), alcohol (0.2 M) and acetic anhydride (0.3 M) in $CH_3CN$. Free energy profiles for the esterification of benzyl alcohol with acetic anhydride in **c** bulk and **d** confined conditions calculated by DFT. Bronsted acid sites are taken as active sites acting as proton sources. The labels TS and IM indicate the transition state and intermediate of the reaction, respectively. The reaction rate is primarily determined by the step from IM1 to TS1, in which the confined energy barrier is clearly smaller than the bulk energy barrier. Error bars represent standard deviation of three measurements.

symmetric matching state between the highest occupied molecular orbital (HOMO) of benzyl alcohol and the lowest unoccupied molecular orbital (LUMO) of protonated acetic anhydride is achieved, favoring the nucleophilic addition reaction. Besides the confinement effect, the intrinsic chemical and electronic structure of catalysts can also affect the molecular reactivity. Specifically, the oxygen vacancies on the surface of $HTiNbO_{5-X}$ nanosheets are considered as Lewis acid sites that also can attract carbonyl oxygen or hydroxyl oxygen assisting molecular polarization, and promote the formation of IM2, as evidenced by the increased adsorption energy of $HTiNbO_{5-X}$ membrane to BnOH and $Ac_2O$. As shown in Supplementary Figs. 33, 34, Lewis acid sites at Nb sites of $HTiNbO_{5-X}$ nanosheets are also counted as active sites for calculation. In this case, the free energy from IM1 to TS1 also delivers an obvious decrease from 47.7 kJ/mol to 39.8 kJ/mol for confined conditions. Compared to that of bulk system, the lower activation energy barriers for reactions in the confined space give rise to a higher-efficiency reaction performance inevitably.

To determine the generality and expansibility of membrane reaction, we further adjust the reactant concentrations, and expand solvents and alcohol derivatives using $HTiNbO_{5-X}$ membranes (d = 11.0 Å) as mentioned above. In Supplementary Fig. 36, the flow volumes are linear with time, and the permeance of reaction solution fall slightly with the concentration increasing (0.1, 0.2, 0.6 and 1.0 M). The experimental results show that the conversion of confined reaction decreases gradually when the concentrations come to 0.6 M and 1.0 M (Supplementary Table 7). This should be ascribed to the saturation of active sites to reactant molecules, since the catalyst dosage of $HTiNbO_{5-X}$ membranes is only 1.68 mg. For bulk reactions, the conversion of benzyl alcohol delivers a completely opposite trend, mainly because the increased probability of molecular collision at high concentrations. In spite of that, the performances of confined reaction are still superior to that of the bulk reaction at the same concentrations. In addition, we have made a comparison of different solvents in terms of boiling point, conversion and flow rate of the reaction solution. When cyclohexane, toluene and chloroform are used as solvents, they also exhibit good conversion rates both in bulk and confined reactions (Supplementary Tables 8, 9). However, flow rates for cyclohexane and toluene are much smaller than acetonitrile in confined reactions, and the reaction time are significantly longer (Supplementary Fig. 37). This can be attributed to the larger size of cyclohexane and toluene, which obstructs their flow within the membranes (Supplementary Fig. 38). Moreover, the $HTiNbO_{5-X}$ membranes are also applied to other alcohol derivatives for corresponding acetate ester flavours, because these ester flavours have attracted special interests in many industrial sectors (Fig. 5, Supplementary Figs. 39–44, Supplementary Table 11). From the Fig. 5 and Supplementary Table 10, these alcohol derivatives exhibited different catalytic activities because

https://doi.org/10.1038/s41467-025-61411-y

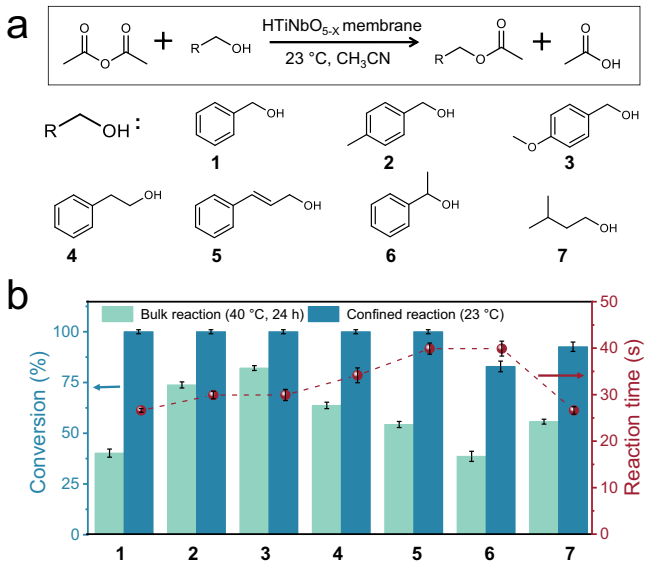


**Fig. 5 | The esterification of acetic anhydride with different alcohol substrates.** **a** Substrate scope. **b** The conversion and reaction time of bulk and confined reactions of different alcohol substrates are compared. Bulk reaction condition: $HTiNbO_{5-X}$ nanosheets (10 mg), alcohol (0.2 M) and acetic anhydride (0.3 M) in $CH_3CN$ at 40 °C for 24 h. Confined reaction condition: $HTiNbO_{5-X}$ membrane (d = 11.0 Å), alcohol (0.2 M) and acetic anhydride (0.3 M) in $CH_3CN$ at 23 °C. Error bars represent standard deviation of three measurements.

of the differences in molecular size, geometric configuration and nucleophilicity. The performance of 1-phenylethyl alcohol and isoamyl alcohol was unsatisfactory, which was speculated to be steric hindrance effect of molecules themselves and mismatch between 2D nanochannel and reactants. Obviously, both the conversion and reaction time of the confined reaction exceed that of bulk reaction, implying $HTiNbO_{5-X}$ membranes are extendable to other different alcohols.

To determine the stability of the membranes, the $HTiNbO_{5-X}$ membranes are tested for four cycles of recyclability test. As shown in Supplementary Fig. 45, the membrane exhibited high stability in both the permeance and conversion of the solution. The conversion of benzyl alcohol remained unchanged at almost 100% for all operation cycles. In Supplementary Fig. 46, we conducted a continuous confined reaction for evaluating reactivity and practicality of the membrane. After more than 13 days of reaction, the products were collected in Supplementary Fig. 46a. According to the theoretical expected product quality, the yield was calculated about 87.5%. The loss of products mainly comes from the processes of filtration reaction and sample collection. The products were also analyzed by $^1H$ NMR spectroscopy, and characteristic signals of benzyl alcohol completely disappeared which means a 100% conversion. The benzyl acetate collected by the confined reaction is almost colorless. To gain insights into stability of oxygen vacancy, XPS spectra of $HTiNbO_{5-X}$ membranes were performed after the long-term stability test. As shown in Supplementary Fig. 47, O 1 s can be divided into three fitting peaks that is lattice oxygen at 530.4 eV, oxygen vacancy at 531.3 eV and organic oxygen at 532.9 eV. Due to the relatively mild reaction conditions, the signal peak of oxygen vacancies did not show any signs of weakening or disappearing. Therefore, it can be confirmed that $HTiNbO_{5-X}$ membranes are very stable during the reaction process.

## Discussion

In summary, $HTiNbO_{5-X}$ LMR with sub-nanoconfined channels was successfully prepared by stacking $V_O$-enriched amorphous/crystalline $HTiNbO_{5-X}$ nanosheets. Such an ingenious atomic architectures endows the $HTiNbO_{5-X}$ LMR with unique electronic and spatial structures along with adjustment of adsorption energy of reactants, molecular polarization and orbital symmetry matching, and reaction thermodynamics. Experimental and theoretical studies clearly revealed the synergistic effect of the oxygen vacancy and the sub-nanoscale confinement to its outstanding performances. Consequently, the $HTiNbO_{5-X}$ membrane reactor exhibits ≈ 100% conversion of benzyl alcohol within 26.6 s under mild conditions, and shows satisfactory stability. Furthermore, this method is applicable for to other alcohol derivatives. This work unraveled the importance of the rational design of metal oxide laminar membrane reactors via synergistically surface defect and spatial confinement strategies. Our work should encourage the adoption of laminar membrane reactors for sustainable chemical synthesis.

## Methods

### Materials

Niobium pentoxide ($Nb_2O_5$, AR), titanium dioxide ($TiO_2$, AR) and cinnamyl alcohol (>98.0%) were commercially supplied by Sigma-Aldrich. Potassium carbonate ($K_2CO_3$, AR), acetic anhydride (>99%), acetonitrile and hydrochloric acid (HCl) were supplied by Sinopharm Chemical Reagent. Amberlyst-15 (Acid siteså 4.7 eq/kg) was supplied by Aladdin. HZSM-5 (Mole ratio of $SiO_2/Al_2O_3$ ≈ 38-40) and $H_3O_{40}PW_{12}{\cdot}xH_2O$ (AR) was supplied by Macklin. Benzyl alcohol (>99.0%), 4-methylbenzyl alcohol (>99.0%), 4-methoxybenzyl alcohol (>98.0%), phenylethyl alcohol (>98.0%), 1-phenylethyl alcohol (>98.0%), 3-methyl-1-butanol (>99.0%) and tetrabutyl ammonium hydroxide (TBAOH, 10 wt%) were purchased from TCI. Dimethyl sulfoxide-d6 (99.8 atom% D, contains 0.03% v/v TMS) was purchased from J&K Scientific. Deionized water (resistivity above 18 MΩ•cm) was collected from a Mili-Q Biocel system. All solvents and reagents were used as received from commercial suppliers unless otherwise indicated.

### Preparation of $HTiNbO_{5-X}$ nanosheets and $HTiNbO_{5-X}$ membranes

The $HTiNbO_{5-X}$ nanosheets were prepared by heating, acid etching, protonation, and exfoliation. $K_2CO_3$ (10.64 g), $TiO_2$ (6.15 g), and $Nb_2O_5$ (10.23 g) were mixed in the mortar. The mixture was annealed in the muffle furnace at 1000 °C for 4 h. After that, the solid sample was collected and ground into powder. The obtained powder was annealed for another 20 hours to fabricate layered $KTiNbO_5$. The $KTiNbO_5$ (2 g) was stirred in HCl (500 mL, 1 M) solution for 3 day, and the solid product was recovered by centrifugation, washed thoroughly with deionized water to remove excess acid and then dried under vacuum. The bulk $HTiNbO_{5-X}$ was obtained via proton exchange and acid etching of $KTiNbO_5$ with HCl aqueous solution for three times. To prepare $HTiNbO_{5-X}$ nanosheets, $HTiNbO_{5-X}$ (500 mg) was soaked in TBAOH dilute solution (100 mL, 1 wt%) for 6 h, and redispersed into 500 mL deionized water, and then exfoliated into nanosheets by mechanical shaking for two weeks. To obtain monolayer $HTiNbO_{5-X}$ nanosheet dispersion (≈ 0.6 mg/mL), the above solution was centrifuged at 3000 revolutions per minute (845 × *g*, 5 min) to remove unstripping $HTiNbO_{5-X}$. The $HTiNbO_{5-X}$ nanosheet dispersion was centrifuged at 12000 revolutions per minute (13523 × *g*, 8 min) to obtain $HTiNbO_{5-X}$ nanosheets powder. The $HTiNbO_{5-X}$ nanosheet powder was thermally treated in vacuum ovens at 60 °C for 12 h.

The $HTiNbO_{5-X}$ membranes were fabricated by vacuum filtration of the $HTiNbO_{5-X}$ nanosheet dispersion. 20 mL $HTiNbO_{5-X}$ nanosheet dispersion (≈ 0.6 mg/mL) was diluted to 100 mL(≈ 0.12 mg/mL), after homogeneous dispersion, and was filtrated with a nylon membrane (47 mm in diameter, pore size of 0.22 μm) as the substrate. The as-prepared $HTiNbO_{5-X}$ membranes were air-dried at 23 °C for 12 h. To regulate interlayer spacing, the membranes were further thermally treated in vacuum ovens at certain temperature (i.e., 40 °C, 60 °C, 80 °C or 100 °C) for 12 h. The membranes with different thicknesses ($HTiNbO_{5-X}$ loadings) were also prepared to investigate their catalytic activity.

### Catalytic evaluation of $HTiNbO_{5-X}$ membranes for the confined reaction

The catalytic reaction was performed in microfiltration devices at room temperature (23 °C) with a measuring cylinder diameter of 15 mm. First, $HTiNbO_{5-X}$ membranes were cut to octagonal shape and fixed onto the surface of a porous glass support, clamping the upper measuring cylinder and the glass support to ensure sealing. Then, acetonitrile ($CH_3CN$) solution containing alcohol (0.2 M) and acetic anhydride (0.3 M) was added to the measuring cylinder, and the measuring cylinder was covered with aluminum foil. The solution flowed through interlayer 2D nanochannels of the membranes driven by a pressure difference (0.9 atm), the reactants reacted in the interlayer, and the products flowed out with the solvent. After removing the solvent from the mixture obtained through membranes by rotary evaporation, dissolving the concentrate with DMSO-D6, analyzing its composition by $^1$H NMR spectroscopy, and calculating the conversion, the reactivity of membrane reactor was compared.

The relevant comparative experiments included the membrane interlayer distances, membrane thicknesses ($HTiNbO_{5-X}$ NS loadings), reaction temperatures, pressure differences, reactant concentrations, solvents and substrates, and overall experiments were conducted analogously.

### Catalytic evaluation of $HTiNbO_{5-X}$ nanosheets for the bulk reaction

The catalytic reaction was performed in 25 mL glass flasks. $HTiNbO_{5-X}$ nanosheet powder (10 mg) was added to acetonitrile solution(10 mL) of alcohol (0.2 M) and acetic anhydride (0.3 M), and the reaction flask was then sealed, stirred and heated at certain temperatures (i.e., 10 °C, 23 °C, 40 °C or 60 °C) for 72 h. Every 24 hours, a specific volume (1 mL) of reaction solution was taken out for testing. After removing the solids by filteration and removing the solvent by rotary evaporation, the obtained concentrate was dissolved in DMSO-D6 and analyzed by $^1$H NMR spectroscopy.

The relevant comparative experiments included the reaction temperatures, reactant concentrations, solvents and substrates, and overall experiments were conducted analogously.

### Recyclability test

The experimental procedures were the same as confined reaction: $HTiNbO_{5-X}$ membranes (d = 11.0 Å), benzyl alcohol (0.2 M) and acetic anhydride (0.3 M) in acetonitrile (10 mL). After the complete filtration of 10 mL of reaction solution (about 100 h), substances flowing through the membranes were collected and analyzed by $^1$H NMR spectroscopy for each cycle. Acetonitrile (2 mL) was utilized to rinse the bottom surface of the membrane and dissolve the substances. The solvent was removed under reduced pressure on a rotary evaporator and the obtained concentrate was dissolved in DMSO-D6. After that, the $HTiNbO_{5-X}$ membranes (d = 11.0 Å) was tested for another cycle, by adding acetonitrile solution (10 mL) of alcohol (0.2 M) and acetic anhydride (0.3 M).

## Data availability

The data that support the findings of this work are available within the article, its supplementary information file (Supplementary Figs. 1–47, Supplementary Tables 1–11), as well as the source data file. The data are also available from the corresponding authors. Source data are provided with this paper.

## References


1. Sá, A. G. A. et al. A review on enzymatic synthesis of aromatic esters used as flavour ingredients for food, cosmetics and pharmaceuticals industries. *Trends Food Sci. Technol.* **69**, 95–105 (2017).
2. Lee, A. F. et al. Heterogeneous catalysis for sustainable biodiesel production via esterification and transesterification. *Chem. Soc. Rev.* **43**, 7887–7916 (2014).
3. Choi, K. R. et al. A microbial process for the production of benzyl acetate. *Nat. Chem. Eng.* **1**, 216–228 (2024).
4. Yao, P. et al. Greener and higher conversion of esterification via interfacial photothermal catalysis. *Nat. Sustain* **5**, 348–356 (2022).
5. Xiao, Q. et al. Ultrafast complete dechlorination enabled by ferrous oxide/graphene oxide catalytic membranes via nanoconfinement advanced reduction. *Nat. Commun.* **15**, 9607 (2024).
6. Grommet, A. B. et al. Chemical reactivity under nanoconfinement. *Nat. Nanotechnol.* **15**, 256–271 (2020).
7. Schreyer, L. et al. Confined acids catalyze asymmetric single aldolizations of acetaldehyde enolates. *Science* **362**, 216–219 (2018).
8. Wang, C. et al. Measuring and modulating substrate confinement during nitrogen-atom transfer in a $Ru_2$-based. *Met.-Org. Framew. J. Am. Chem. Soc.* **141**, 19203–19207 (2019).
9. Ge, H. et al. A tandem catalyst with multiple metal oxide interfaces produced by atomic layer deposition. *Angew. Chem. Int. Ed.* **55**, 7081–7085 (2016).
10. Lei, F. et al. Metallic tin quantum sheets confined in graphene toward high-efficiency carbon dioxide electroreduction. *Nat. Commun.* **7**, 12697 (2021).
11. Nothling, M. D. et al. Synthetic catalysts inspired by hydrolytic enzymes. *ACS Catal.* **9**, 168–187 (2019).
12. Xu, X. et al. High-efficiency $CO_2$ separation using hybrid LDH-polymer membranes. *Nat. Commun.* **12**, 3069 (2021).
13. Tang, L. et al. Confinement catalysis with 2D materials for energy conversion. *Adv. Mater.* **31**, 1901996 (2019).
14. Zou, Y. et al. Enhanced organic photocatalysis in confined flow through a carbon nitride nanotube membrane with conversions in the millisecond regime. *ACS Nano* **15**, 6551–6561 (2021).
15. Meng, C. et al. Angstrom-confined catalytic water purification within Co-$TiO_x$ laminar membrane nanochannels. *Nat. Commun.* **13**, 4010 (2022).
16. Lu, N. et al. Tempospatially confined catalytic membranes for advanced water remediation. *Adv. Mater.* **36**, 2311419 (2024).
17. Fu, Q. et al. Surface chemistry and catalysis confined under two-dimensional materials. *Chem. Soc. Rev.* **46**, 1842–1874 (2017).
18. Gutmann, B. et al. Continuous-flow technology-a tool for the safe manufacturing of active pharmaceutical ingredients. *Angew. Chem. Int. Ed.* **54**, 6688–6728 (2015).
19. Pang, S. et al. Regulating interlayer spacing of aminated graphene oxide membranes for efficient flow reactions. *Matter* **6**, 1173–1187 (2023).
20. Li, X. et al. Efficient flow synthesis of aspirin within 2D sub-nanoconfined laminar annealed graphene oxide membranes. *Adv. Mater.* **36**, 2310954 (2024).
21. Verma, R. et al. Defects tune the acidic strength of amorphous aluminosilicates. *Nat. Commun.* **15**, 6899 (2024).
22. Yang, M. et al. Disorder engineering in monolayer nanosheets enabling photothermic catalysis for full solar spectrum (250–2500nm) harvesting. *Angew. Chem. Int. Ed.* **58**, 3077–3081 (2019).
23. Bi, F. et al. Engineering triple O-Ti-O vacancy associates for efficient water-activation catalysis. *Nat. Commun.* **16**, 851 (2025).
24. Shen, L. et al. Ultrathin $Ti_2Nb_2O_9$ nanosheets with pseudocapacitive properties as superior anode for sodium ion batteries. *Adv. Mater.* **30**, 1804378 (2018).
25. Wang, Y. et al. Ammonia electrosynthesis from nitrate using a stable amorphous/crystalline dual-phase Cu catalyst. *Nat. Commun.* **16**, 897 (2025).
26. Li, R. et al. Amorphization-induced surface electronic states modulation of cobaltous oxide nanosheets for lithium-sulfur batteries. *Nat. Commun.* **12**, 3102 (2021).

27. Qin, Q. et al. Constructing interfacial oxygen vacancy and ruthenium Lewis acid-base pairs to boost the alkaline hydrogen evolution reaction kinetics. *Angew. Chem. Int. Ed.* **63**, e202317622 (2024).
28. Guo, Z. et al. Crystallinity engineering for overcoming the activity-stability tradeoff of spinel oxide in Fenton-like catalysis. *Proc. Natl Acad. Sci. USA.* **120**, e2220608120 (2023).
29. Chen, X. et al. Effect of adsorbed water molecules on the surface acidity of niobium and tantalum oxides studied by mas NMR. *J. Phys. Chem. C.* **125**, 9330–9341 (2021).
30. Nakajima, K. et al. Titania as an early transition metal oxide with a high density of Lewis. *acid sites workable water J. Phys. Chem. C.* **117**, 16028–16033 (2013).
31. Zhang, X. et al. Adsorption and separation of ethyl mercaptan from methane by hydroxyl groups on the surface of $HTiNbO_5$-nanosheets. *Langmuir* **38**, 1497–1508 (2022).
32. Zhang, H. et al. A combo Zr-HY and Al-HY zeolite catalysts for the one-pot cascade transformation of biomass-derived furfural to γ-valerolactone. *J. Catal.* **375**, 56–67 (2019).
33. Zhang, J. et al. Control of interfacial acid–metal catalysis with organic monolayers. *Nat. Catal.* **1**, 148–155 (2018).
34. Du, X. et al. Selective nucleophilic α-C alkylation of phenols with alcohols via $Ti{=}C_\alpha$ intermediate on anatase $TiO_2$ surface. *Nat. Commun.* **14**, 4479 (2023).
35. Sripada, S. et al. Continuous catalytic esterification using a solid acid activated carbon monolith: Comparison of granular and monolith forms with a commercial catalyst. *Chem. Eng. J.* **476**, 146586 (2023).
36. Su, F. et al. Advancements in solid acid catalysts for biodiesel production. *Green. Chem.* **16**, 2934 (2014).
37. Lu, Q. How to correctly analyze 2p X-ray photoelectron spectra of 3d transition-metal oxides: pitfalls and principles. *ACS Nano* **18**, 13973–13982 (2024).
38. Nakajima, K. et al. $Nb_2O_5{\cdot}nH_2O$ as a heterogeneous catalyst with water-tolerant lewis acid sites. *J. Am. Chem. Soc.* **133**, 4224–4227 (2011).
39. Siddiki, S. M. A. H. et al. Lewis acid catalysis of $Nb_2O_5$ for reactions of carboxylic acid derivatives in the presence of basic inhibitors. *ChemCatChem* **11**, 383–396 (2019).
40. Kreissl, H. T. et al. Structural studies of bulk to nanosize niobium oxides with correlation to their acidity. *J. Am. Chem. Soc.* **139**, 12670–12680 (2017).
41. Xin, Y. et al. Correlation of the catalytic performance with $Nb_2O_5$ surface properties in the hydrodeoxygenation of lignin model compound. *J. Catal.* **375**, 202–212 (2019).
42. Yang, L. et al. Stabilizing Pt electrocatalysts via introducing reducible oxide support as reservoir of electrons and oxygen species. *ACS Catal.* **12**, 13523–13532 (2022).
43. Brayner, R. et al. Niobium pentoxide prepared by soft chemical routes: morphology, structure, defects and quantum size effect. *Phys. Chem. Chem. Phys.* **5**, 1457–1466 (2003).
44. Yu, X. et al. Highly enhanced photoactivity of anatase $TiO_2$ nanocrystals by controlled hydrogenation-induced surface defects. *ACS Catal.* **3**, 2479–2486 (2013).
45. Livraghi, S. et al. Nature of reduced states in titanium dioxide as monitored by electron paramagnetic resonance. II. *rutile brookite cases. J. Phys. Chem. C.* **118**, 22141–22148 (2014).
46. Dai, J. et al. Spin polarized $Fe_1$-Ti pairs for highly efficient electroreduction nitrate to ammonia. *Nat. Commun.* **15**, 88 (2024).
47. Pfriem, N. et al. Role of the ionic environment in enhancing the activity of reacting molecules in zeolite pores. *Science* **372**, 952–957 (2021).
48. Ji, P. et al. Strongly lewis acidic metal-organic frameworks for continuous flow catalysis. *J. Am. Chem. Soc.* **141**, 14878–14888 (2019).
49. Xue, Z. et al. Tuning the adsorption energy of methanol molecules along Ni-N-doped carbon phase boundaries by the mott-schottky effect for gas-phase methanol dehydrogenation. *Angew. Chem. Int. Ed.* **57**, 2697–2701 (2018).
50. Collins, S. E. et al. Acylating capacity of the phosphotungstic Wells-Dawson heteropoly acid: intermediate reactive species. *J. Phys. Chem. C.* **115**, 700–709 (2011).
51. Bachiller-Baeza, B. et al. FTIR and reaction studies of the acylation of anisole with acetic anhydride over supported HPA catalysts. *J. Catal.* **228**, 225–233 (2004).


## Acknowledgements

This work was supported by the National Key R&D program of China (Grant No. 2021YFA1200402 to X.Z.), the Beijing Natural Science Foundation (Grant No. 2252057 to X.Z.), and the National Natural Science Foundation of China (Grant Nos. 52373219 to X.Z. and 21988102 to L.J.).

## Author contributions

X. Zhang and L. Jiang conceived the idea and directed the study. Z. Fang performed the main experiments and drafted the manuscript. X. Li, Y. Zhang and G. He participated in the experiments for sample characterization. Y. Bai and D. Peng contributed to the computational studies. Y. Bai, S. Pang and F. Xia helped with data analysis and manuscript polishing. All authors participated in the interpretation of the data and production of the final paper.

## Competing interests

The authors declare no competing interests.

## Additional information

**Supplementary information** The online version contains supplementary material available at https://doi.org/10.1038/s41467-025-61411-y.

**Correspondence** and requests for materials should be addressed to Xiqi Zhang.

**Peer review information** *Nature Communications* thanks Milad Abolhasani, and the other, anonymous, reviewer(s) for their contribution to the peer review of this work. A peer review file is available.